Article

Two annual cycles of the Pacific cold tongue under orbital precession

https://doi.org/10.1038/s41586-022-05240-9

Received: 19 April 2022

Accepted: 16 August 2022

Published online: 9 November 2022

Check for updates

John C. H. Chiang[1,2]✉, Alyssa R. Atwood[3], Daniel J. Vimont[4], Paul A. Nicknish[5], William H. G. Roberts[6], Clay R. Tabor[7] & Anthony J. Broccoli[8]

The Pacific cold tongue annual cycle in sea surface temperature is presumed to be driven by Earth's axial tilt[1–5] (tilt effect), and thus its phasing should be fixed relative to the calendar. However, its phase and amplitude change dramatically and consistently under various configurations of orbital precession in several Earth System models. Here, we show that the cold tongue possesses another annual cycle driven by the variation in Earth–Sun distance (distance effect) from orbital eccentricity. As the two cycles possess slightly different periodicities[6], their interference results in a complex evolution of the net seasonality over a precession cycle. The amplitude from the distance effect increases linearly with eccentricity and is comparable to the amplitude from the tilt effect for the largest eccentricity values over the last million years (*e* value approximately 0.05)[7]. Mechanistically, the distance effect on the cold tongue arises through a seasonal longitudinal shift in the Walker circulation and subsequent annual wind forcing on the tropical Pacific dynamic ocean–atmosphere system. The finding calls for reassessment of current understanding of the Pacific cold tongue annual cycle and re-evaluation of tropical Pacific palaeoclimate records for annual cycle phase changes.

The Pacific cold tongue is an integral part of the tropical Pacific coupled ocean–atmosphere system and possesses a dominant annual cycle in sea surface temperature (SST) (Extended Data Fig. 1), even though insolation at the equator peaks twice a year[1](Extended Data Fig. 2a). Prevailing theory developed in the 1990s[1–5] explained the annual cycle through the following sequence: an annual mean equatorial cold tongue arises through easterly trade winds which shallow the thermocline to the east, allowing upwelling to bring cold water from below the thermocline into the mixed layer[8]. Because of the northward bias of the Pacific Intertropical Convergence Zone[9] southeasterly trade winds cross the equator throughout the year. Their strength changes over the course of a year, controlled by the differential heating between hemispheres resulting from the tilt effect, with a delay due to the thermal inertia of the ocean. The southeasterly trade winds are strongest in boreal autumn (Extended Data Fig. 1b) and cause surface waters to cool at the eastern boundary through coastal upwelling that propagates westwards along the equator, facilitated by zonal ocean–atmosphere feedback[10,11]; the same winds also drive increased surface heat fluxes and vertical mixing at the equator, further cooling the equatorial surface ocean[3,10]. Conversely, when the southeasterly trade winds weaken in boreal spring, the cold tongue is warmer (Extended Data Fig. 1c). Because the cold tongue annual cycle is controlled by the tilt effect, its phase relative to the calendar year should be relatively immutable as both are timed to the equinoxes.

This prevailing view was recently challenged by an Earth system model[12] (Geophysical Fluid Dynamics Laboratory (GFDL) CM 2.1; Methods) simulating a remarkable change in the phase of the cold tongue annual cycle with the longitude of perihelion (the position of perihelion relative to the moving vernal equinox as shown in Fig. 1; hereafter LOP). The eccentricity was set to 0.0493, being the maximum attained over the last 600,000 years[7] and about three times as large as the modern-day value (Extended Data Fig. 2b). When the LOP was altered from 90° (perihelion at winter solstice) to 180° (perihelion at vernal equinox), the coldest month changed from August to October; then to January for LOP at 270° (perihelion at summer solstice) and then to May for LOP at 0° (perihelion at autumnal equinox) (Fig. 2, top row). The amplitude of the annual cycle also changed dramatically, being largest for LOP at 90° and 180° and smallest with LOP at 0°, despite obliquity being fixed. No straightforward relationship is discernible when the cold tongue annual cycle behaviour is compared with its corresponding seasonal cycle of insolation at the equator (Extended Data Fig. 2c–f). Similar cold tongue behaviour is found in identical sets of simulations performed with two other Earth System models (iCESM 1.2 and HadCM3) (Fig. 2, second and third rows, respectively) and with a fourth model (EC Earth; Extended Data Fig. 3) performed with slightly different orbital parameters (Methods section on 'Earth System Model simulations').

[1]Department of Geography, University of California, Berkeley, CA, USA. [2]Research Institute for Environmental Changes, Academia Sinica, Taipei, Taiwan ROC. [3]Department of Earth, Ocean, and Atmospheric Sciences, Florida State University, Tallahassee, FL, USA. [4]Department of Atmospheric and Oceanic Sciences, University of Wisconsin-Madison, Madison, Madison, WI, USA. [5]Department of Earth and Planetary Science, University of California, Berkeley, CA, USA. [6]Department of Geography and Environmental Science, Northumbria University, Newcastle-upon-Tyne, UK. [7]Department of Geosciences, University of Connecticut, Storrs, CT, USA. [8]Department of Environmental Sciences, Rutgers University, New Brunswick, NJ, USA. ✉e-mail: jch_chiang@berkeley.edu

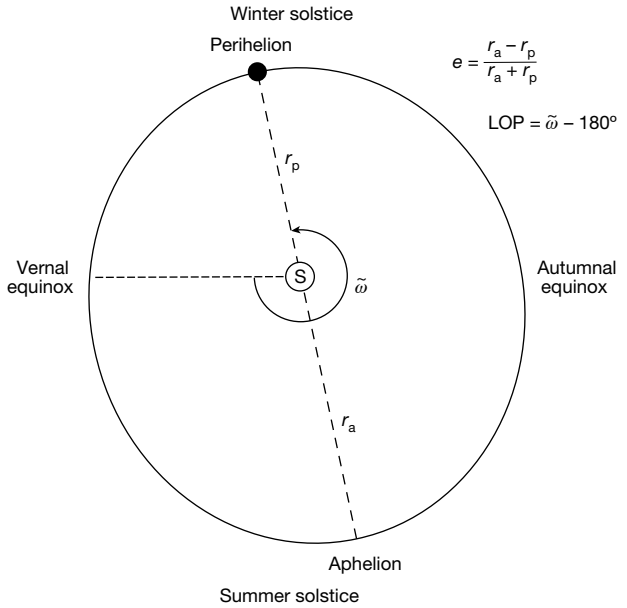

Fig. 1 | Schematic of the Earth's orbital configuration. The Earth's orbit around the Sun (marked S) is elliptical with the Sun at one focal point and with the closest approach at perihelion (at a distance r_p) and furthest at aphelion (r_a). The direction of the orbit is counterclockwise. The eccentricity e, defined in the figure, measures how elliptical the orbit is: $e = 0.0493$ is used for the simulations reported in Fig. 2, about three times larger than the modern-day value. The equinox and solstice points are named following Northern hemisphere seasons. The LOP relative to the moving vernal equinox is defined (following Fig. 8 of ref. [38]) as the angular distance from vernal equinox to perihelion following Earth's orbit ($\tilde{\omega}$, in degrees), subtracted by 180°. Thus, LOP is 90° and 180° if perihelion occurs during winter solstice and vernal equinox, respectively. Perihelion, as drawn in the schematic, is positioned for modern day, with an LOP of about 103° and date of around 3 January. Because the distance effect annual cycle (from perihelion to perihelion, otherwise called the anomalistic year, 365.259636 d (ref. [6])) is slightly longer than the tilt effect annual cycle (from equinox to equinox, otherwise known as the tropical year, 365.242189 d (ref. [6])), the LOP increases over time. A complete revolution of the LOP is the precession cycle, about 22,000 yr (ref. [38]). Note that the Gregorian calendar is referenced to the vernal equinox, with its rule for leap days designed to resynchronize the calendar year with the tropical year.

Cold tongue response to eccentricity

When eccentricity is set to zero and annual cycle forcing arises solely from the tilt effect, the simulated Pacific cold tongue seasonality behaves in a way that is consistent with prevailing theory, with the cold peak timed to boreal autumn and warm peak to boreal spring (Fig. 2, last column). We show that as orbital eccentricity is introduced, another cold tongue annual cycle emerges. Simulations with an Earth system model (Community Earth System Model (CESM) 1.2; Methods section on 'Earth System Model simulations) spanning the range of LOP are undertaken at three eccentricities (e)—0.01, 0.02 and 0.04—covering the typical range over the last million years[7] (hereafter the CESM LOP simulations; Methods section on 'Earth System Model simulations). All other boundary conditions are set to pre-industrial levels (1850 AD), including obliquity.

The cold tongue annual cycle shows two distinct features as the longitude of perihelion is varied (Fig. 3a; for $e = 0.04$): a change in the timing of peaks and troughs and a marked reduction in amplitude near LOP = 0°. We fit the results of Fig. 3a with the sum of two cosines, one whose phase is fixed to the calendar representing the tilt effect and the other whose phase changes linearly with the LOP representing the distance effect. We also include a semi-annual cycle with its phase fixed to the calendar, to account for insolation peaking at the equator twice a year during the equinoxes (Extended Data Fig. 2a).

$$\mathrm{CT_{fit}} = A_\mathrm{T}\cos\left(\left(\frac{2\pi}{12}\right)(m - p_\mathrm{T})\right) + A_\mathrm{D}\cos\left(\left(\frac{2\pi}{12}\right)(m - p_\mathrm{D}) - \left(\frac{\mathrm{LOP}\pi}{180}\right)\right) + A_\mathrm{S}\cos\left(\left(\frac{2\pi}{6}\right)(m - p_\mathrm{S})\right) \quad (1)$$

in which $\mathrm{CT_{fit}}$ is the modelled cold tongue sea surface temperature (with annual cycle removed), A_T and p_T are the amplitude and phase of the annual cycle for the tilt effect, A_D and p_D for the distance effect and A_S and p_S for the semi-annual cycle. Parameter m is the numerical months of the year from 0 to 12 (with 0.5 corresponding to mid-January) and LOP is in degrees.

The best-fit surface to the data (Fig. 3b; Methods section on 'Surface fitting') captures its salient features, including the change in phase and reduction in amplitude near LOP = 0°. The tilt and distance annual cycles are comparable in amplitude (Fig. 3d,e) but the semi-annual contribution is relatively small (Fig. 3f). The same fitting exercise but with $e = 0.01$ and 0.02 (Extended Data Fig. 4) shows an essentially unchanged annual cycle contribution from the tilt effect and semi-annual cycle (Table 1) but the amplitude of the distance effect annual cycle decreases linearly with decreasing eccentricity (Fig. 3c). A similar outcome occurs when fitting equation (1) to a simulation with $e = 0$ (the tilt-only run), assuming $A_\mathrm{D} = 0$ (Table 1). The consistency in the fitted parameters lends confidence to the validity of our model.

The above results are consistent with cold tongue seasonality arising from the sum of the tilt and distance effect annual cycles. As the duration of the distance effect annual cycle is slightly longer than that of the tilt effect (at present by about 25 min)[6], the two interfere resulting in a complex evolution of the net cold tongue annual cycle with orbital precession. The amplitude from the distance effect increases linearly at around 0.23 K per 0.01 eccentricity units (Fig. 3c), meaning that even at today's low eccentricity the amplitude from the distance effect is about one-third of that from the tilt effect. For the largest orbital eccentricities over the last million years ($e > 0.05$) (ref. [7]), the distance effect amplitude is as large or even larger than the tilt effect amplitude.

We confirm this interpretation through a simulation that removes the tilt effect by setting obliquity to 0° (the distance-only run); we use $e = 0.05$ (and LOP = 0°) such that the distance effect amplitude approximately matches the tilt effect amplitude. In contrast to the annual cycle in the tilt-only run (Extended Data Fig. 5c), the distance-only run shows an annual cycle with a cold peak in early May and warm peak in mid-late October (Extended Data Fig. 5b). When the two annual cycles are summed, they produce a cold tongue seasonality which resembles the simulation with both distance and tilt effects present (Extended Data Fig. 5a,d). With both eccentricity and obliquity set to zero (the zero annual forcing run), the cold tongue annual cycle essentially disappears (Extended Data Fig. 5e).

Equatorial wind and thermocline changes

Previous model studies using mid-Holocene orbital conditions (corresponding to LOP of about 0°)[12–14] have suggested that the cold tongue annual cycle changes are dynamically induced through equatorial thermocline changes. Ref. [12] shows in a LOP = 0° simulation that, in boreal spring, weakening trade winds in the western equatorial Pacific coincide with a deeper equatorial thermocline, the last of which propagates eastwards to warm the eastern equatorial SST by boreal autumn. Thermodynamic SST changes by direct insolation forcing also contribute to the autumn warming. The opposite occurs for the other half of the year. We note that the prevailing theory for the cold tongue annual cycle does not prescribe a role to seasonal variations in the thermocline[2].

We similarly examine equatorial wind stress and thermocline changes in the CESM LOP simulations. Using the $e = 0.04$ case, we find a clear eastward propagation of the thermocline anomaly originating from

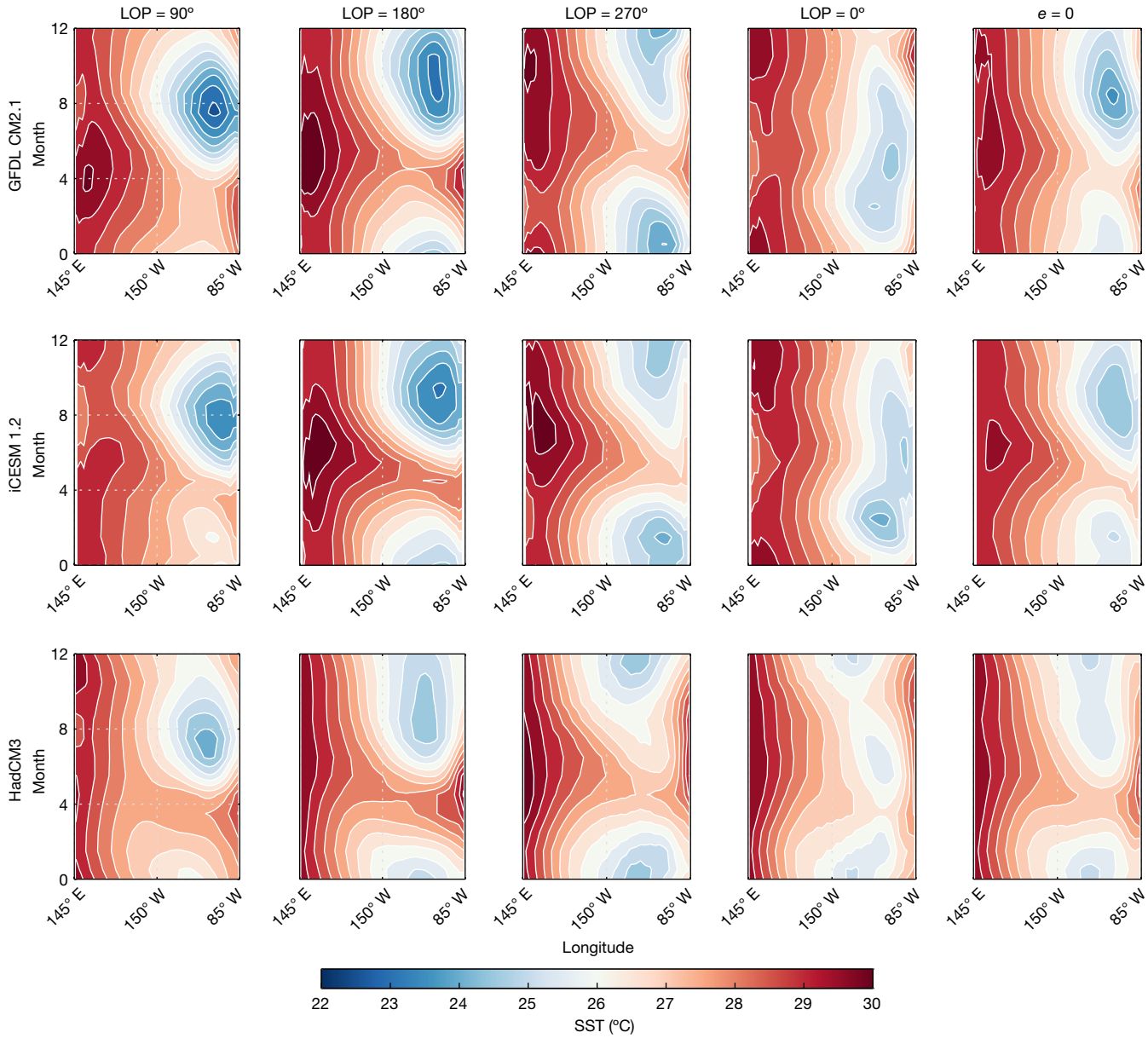

Fig. 2 | Annual cycles of equatorial Pacific SSTs for three different Earth System models show a remarkable and consistent seasonal variation with the LOP. Plotted is the climatological monthly mean SST averaged over 6° S–6° N, for GFDL CM 2.1 (ref. [12]) (top row), iCESM 1.2 (ref. [40]) (second row) and HadCM3 (third row). The numbers on the top row denote the LOP (for which 90° is perihelion at winter solstice, 180° at vernal equinox, 270° at summer solstice and 0° at autumnal equinox). The last column ($e = 0$) denotes simulations with eccentricity set to zero. To facilitate comparison, an offset is added to each panel so that the annual mean SST averaged over 145° E–85° W is the same as for the observational data, as shown in Extended Data Fig. 1a, 27.44 °C. Note that the time (y) axis here and in other figures is such that 0 is the start of the year and 12 is the end; mid-January is thus 0.5.

the western Pacific for all LOP cases, provided that the tilt effect contribution is removed beforehand (Extended Data Fig. 6, contours). Zonal wind stress changes in the western equatorial Pacific precede thermocline anomalies for all LOP cases, with anomalous westerlies corresponding to a deeper thermocline and vice versa (Extended Data Fig. 6, shaded). Thus, the distance effect annual cycle seems to involve the same coupled ocean–atmosphere dynamics and equatorial thermocline propagation that gives rise to the El Nino/Southern Oscillation (ENSO)[15].

We confirm this interpretation using a set of simplified model simulations (Methods section on 'Simulations with an ICM of the tropical Pacific'). First, we obtain the distance effect wind response by imposing the appropriate orbital conditions (and LOP = 0°) in CESM 1.2 with the ocean component replaced by a 'slab' ocean that incorporates thermodynamic ocean–atmosphere interactions from surface fluxes but not the dynamical thermocline evolution. They generate a seasonal cycle of zonal wind anomalies in the equatorial western Pacific that is independent of the dynamic ocean–atmosphere coupling, with peak anomalous westerlies occurring at the end of April (Extended Data Fig. 7a). These winds are then imposed as an annually repeating forcing on an intermediate coupled model[16] (ICM) which contains the essential dynamics to simulate the ENSO. The ICM responds by producing a cold tongue annual cycle with the peak warm phase occurring 3–4 months after the peak anomalous westerlies in the western Pacific (Extended Data Fig. 7a). As in the CESM LOP simulations, eastward-propagating thermocline variations link the zonal wind annual cycle in the western Pacific to the annual cycle of the cold tongue in the ICM (Extended Data Fig. 7b). We conclude that the coupled dynamics that generate

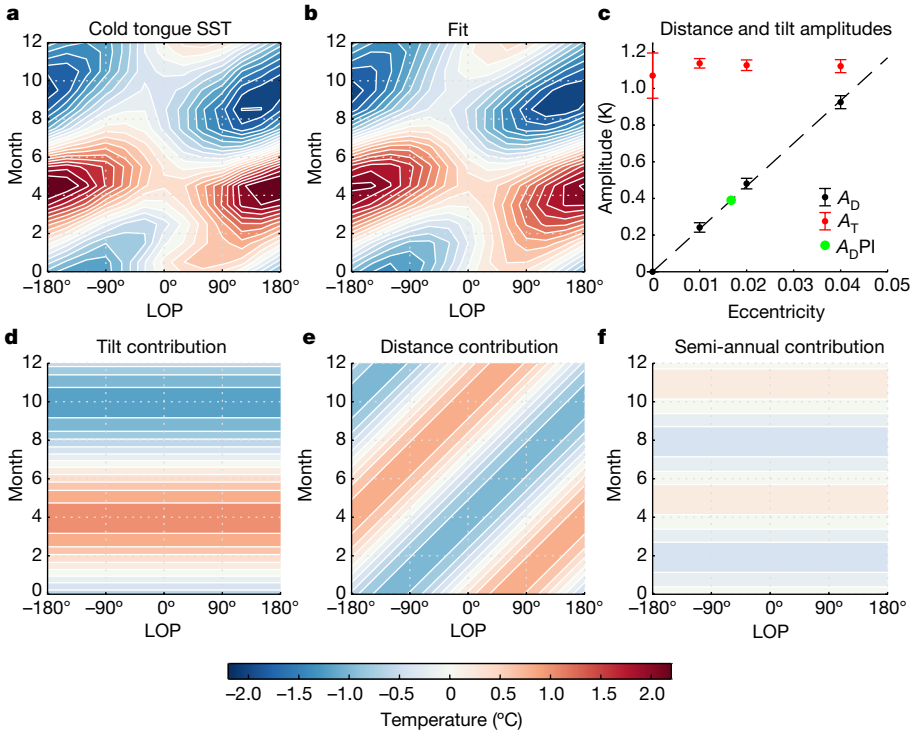

Fig. 3 | Variation of the cold tongue annual cycle to LOP arises from the sum of the tilt and distance effect contributions. a, Cold tongue SST (averaged over 6° S–6° N, 140–90° W) annual cycle for $e = 0.04$ with varying longitude of perihelion. The annual mean is removed from each annual cycle before plotting. **b**, Least-square surface fit of the data in **a**, using equation (1). **c**, Fitted coefficients of the distance effect amplitude (A_D, black symbols) and the least-square linear fit to the data forced through the intercept (dashed line). The bars indicate the 95% confidence bounds for each A_D fit. For comparison, the fitted coefficients of the tilt effect amplitude (A_T) are shown in red. The green dot indicates the distance effect amplitude for eccentricity at pre-industrial (PI) level ($e = 0.0167$). **d**–**f**, Contributions of the fit in **b** from tilt effect (**d**), distance effect (**e**) and semi-annual cycle (**f**) . The same colour scale is used for **a**, **b**, **d**, **e** and **f**.

ENSO are also integral to the distance effect cold tongue annual cycle. These coupled dynamics arise as a forced response to the annual cycle in zonal wind stress changes in the western Pacific which arise from a thermodynamic response to the distance effect.

The peak warm phase of the cold tongue in the distance-only run occurs 4–5 months after the peak anomalous westerlies (Extended Data Fig. 5b), a longer lag time than in the ICM (Extended Data Fig. 7a). We attribute this difference to the direct thermodynamic response of the distance effect insolation on SST, which has its peak warm phase about 7 months after the peak westerlies (Extended Data Fig. 7c); this would act to delay the timing of the warm peak in the cold tongue.

Table 1 | Fitted coefficients for equation (1) to the cold tongue SST annual cycle variation with LOP in the CESM LOP simulations, for various eccentricity values

Eccentricity (e)	A_T (K)	p_T (month)	A_D (K)	p_D (month)	A_S (K)	p_S (month)
0.00	1.07 (0.95, 1.19)	4.02 (3.80, 4.25)	0	-	0.33 (0.21, 0.46)	5.07 (4.71, 5.42)
0.01	1.14 (1.11, 1.16)	4.03 (3.99, 4.08)	0.24 (0.22, 0.27)	10.13 (9.92, 10.33)	0.31 (0.29, 0.34)	5.00 (4.92, 5.08)
0.02	1.13 (1.10, 1.16)	4.01 (3.96, 4.06)	0.48 (0.45, 0.51)	10.08 (9.97, 10.20)	0.32 (0.29, 0.35)	4.98 (4.90, 5.07)
0.04	1.12 (1.09, 1.16)	3.94 (3.88, 4.00)	0.93 (0.89, 0.96)	10.02 (9.95, 10.10)	0.32 (0.29, 0.36)	4.90 (4.79, 5.00)

The cold tongue SST is averaged over 140–90° W, 6° S–6° N. For zero eccentricity, A_D is assumed to be zero. The values in brackets indicate the 95% confidence bounds. Note the consistency in the coefficients for A_T, A_S, p_T, p_S and p_D across various eccentricities.

Zonal shift in the Walker circulation

The western Pacific wind changes result from a seasonal cycle in the longitudinal position of the Walker circulation driven by the distance effect. In the distance-only run, the equatorial easterlies in the western Pacific exhibit an annual cycle and essentially vanish between March and June (Fig. 4a, black contours). This feature contrasts with the zero annual forcing run in which the equatorial Pacific zonal winds are always easterly. The cold tongue is at its coldest (Fig. 4a, shaded) when the easterlies vanish, indicating that the winds are not being driven by the cold tongue SST. Rather, the vanishing easterlies result from an eastward shift of the main uplift region of the Walker circulation (Extended Data Fig. 8c), accompanied by an increase in the precipitation over the equatorial western Pacific and decrease over the Maritime Continent (Extended Data Fig. 8a). The opposite occurs during September–December (Extended Data Fig. 8b,d).

We use an atmospheric energy flux analysis[17] to confirm the Walker circulation shift and diagnose its causes (Methods section on 'Atmospheric energy flux analysis'). This analysis links the longitude of its main uplift region to the position of zero and diverging zonal energy flux, otherwise known as the energy flux prime meridian (EFPM). For the zero annual forcing run, the EFPM over the equatorial western Pacific stays at about 150° E throughout the year (Fig. 4a, green dashed line). With eccentricity increased to 0.05, a distance effect annual cycle in the EFPM emerges with an eastward shift between March and June following aphelion and a westward shift between September and December following perihelion (Fig. 4a, green solid line); note that it aligns

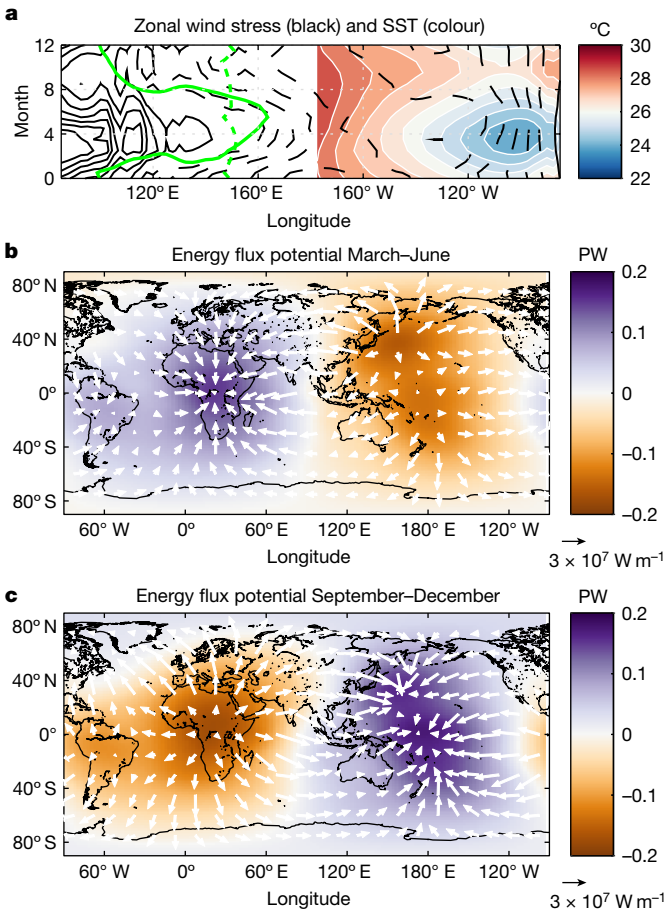

Fig. 4 | The distance effect on the longitude position of the Walker circulation as diagnosed by the energy flux potential. a, Equatorial Pacific zonal wind stress (black contours, contour interval 1×10^{-2} N m^{-2}; dashed contours are negative and zero contour not shown) and SST (shaded) averaged over 6° S–6° N for the distance-only run (obliquity = 0°, e = 0.05, LOP = 0°). Positive values of wind stress correspond to westerly winds. Because the focus is on the cold tongue, SST is only shown east of the date line; also, an offset is added so that the annual mean SST averaged over 145° E–85° W is the same as for the observational data, as shown in Extended Data Fig. 1a, 27.44 °C. The solid green line shows the EFPM over the western Pacific for the distance-only run and the dashed green line for the zero annual forcing run. **b**, Energy flux potential (shaded, units are petawatts (PW)) averaged over March–June, for the difference between the distance-only and zero annual forcing runs (the former minus the latter). The vectors correspond to the difference in the divergent horizontal atmospheric energy transport. **c**, Same as **b** but for September–December. See Methods section on 'Atmospheric energy flux analysis' for details on the calculations. The M_Map package[41] was used to generate the maps in **b** and **c**, using coastline data from the global self-consistent, hierarchical, high-resolution geography database[42].

well with the zonal wind stress changes over the western equatorial Pacific. The EFPM change is caused by a zonal dipole in the energy flux potential (Fig. 4b,c, shading) between the hemisphere extending from the Maritime Continent through the Pacific (the marine hemisphere, being mostly ocean), with the hemisphere extending from South America through to the Indian Ocean (the continental hemisphere, having relatively more land). For March–June following aphelion, there is increased zonal atmospheric energy transport from the marine to the continental hemisphere (Fig. 4b, vectors) and the EFPM (and hence the Walker uplift region) shifts eastwards. The opposite occurs in September–December following perihelion (Fig. 4c). Other diagnostics of the large-scale atmospheric circulation—upper tropospheric velocity potential and surface pressure—confirm the seasonal zonal shift in the Walker circulation and the global east–west hemispheric nature of its origins (Extended Data Fig. 8e–h).

The zonal energy transport arises from the differing thermal response of the two hemispheres to the distance effect. For September–December following perihelion, the surface of the marine hemisphere absorbs relatively more of the increased sunlight than that of the continental hemisphere, implying that the marine hemisphere fluxes less energy into the overlying atmosphere than the continental hemisphere. Because tropical atmospheric dynamics act to rapidly homogenize tropospheric temperature differences[18], there is increased zonal atmospheric energy transport from the continental to the marine hemisphere and the Walker circulation shifts to the west. The opposite occurs in March–June following aphelion. This behaviour is analogous to the latitudinal migration of the Intertropical Convergence Zone in response to atmospheric energy transport changes between the northern and southern hemispheres from the tilt effect[19,20].

Implications

Our findings call for a re-evaluation of mechanisms underpinning the Pacific cold tongue annual cycle, in particular thermocline changes. The distance effect may have escaped attention as the current annual cycle resembles that from the tilt effect alone and thus does not pose a challenge to the prevailing theory. It also begs the question: to what extent does the distance effect contribute to the seasonal cycle of other regional climates? This question is rarely asked[21] but this study demonstrates how new insights about the Earth's seasonal cycle are made possible if the tilt and distance effects are considered separately.

We also argue for a re-examination of tropical Pacific palaeoclimate records for changes to the annual cycle. Palaeoclimate studies examining tropical Pacific records on orbital timescales have largely framed cold tongue changes in terms of ENSO[22–27], although attempts have been made to separate amplitude changes into ENSO and annual cycle contributions[25,28–30]. Determining the phasing of palaeoproxy signals relative to the calendar year is more challenging and we are not aware of any attempts in this regard. It requires records that resolve the annual cycle and a marker to affix the calendar. The semi-annual cycle can potentially serve as a marker, as it is timed to equinoxes. We also note that a change in the cold tongue annual cycle may itself cause changes to ENSO because feedbacks that govern the latter depend on the seasonal cycle[31,32].

Finally, we speculate on the implications to the global palaeoclimate. The tropical Pacific is thought to play a defining role in palaeoclimate on orbital timescales[33,34], given its responsiveness to forcing and global reach through teleconnections. The phase of precession has been linked to many regional palaeoclimate changes around the globe, prominent examples being peak monsoon intensity[35,36] and the timing of the Ice Ages[37–39]. The implicit assumption is that the precession influence works through direct insolation changes at the latitude of the regional climate. However, our results indicate that the tropical Pacific may also be capable of remotely orchestrating precession changes around the globe, through altering the cold tongue annual cycle.

Online content

Any methods, additional references, Nature Research reporting summaries, source data, extended data, supplementary information, acknowledgements, peer review information; details of author contributions and competing interests; and statements of data and code availability are available at https://doi.org/10.1038/s41586-022-05240-9.

1. Mitchell, T. P. & Wallace, J. M. The annual cycle in equatorial convection and sea-surface temperature. *J. Clim.* **5**, 1140–1156 (1992).
2. Xie, S. P. On the genesis of the equatorial annual cycle. *J. Clim.* **7**, 2008–2013 (1994).
3. Chang, P. The role of the dynamic ocean–atmosphere interactions in the tropical seasonal cycle. *J. Clim.* **9**, 2973–2985 (1996).

4. Li, T. M. & Philander, S. G. H. On the annual cycle of the eastern equatorial Pacific. *J. Clim.* **9**, 2986–2998 (1996).
5. Wang, B. On the annual cycle in the Tropical Eastern Central Pacific. *J. Clim.* **7**, 1926–1942 (1994).
6. United States Nautical Almanac Office, United States Naval Observatory, Her Majesty's Nautical Almanac Office and the United Kingdom Hydrographic Office. *The Astronomical Almanac for the Year 2019* (United States Government Printing Office, 2019).
7. Berger, A. & Loutre, M. F. Insolation values for the climate of the last 10000000 years. *Quat. Sci. Rev.* **10**, 297–317 (1991).
8. Xie, S. P. & Philander, S. G. H. A. Coupled ocean–atmosphere model of relevance to the ITCZ in the Eastern Pacific. *Tellus* **46**, 340–350 (1994).
9. Philander, S. G. H. et al. Why the ITCZ is mostly north of the equator. *J. Clim.* **9**, 2958–2972 (1996).
10. Xie, S. P. Westward propagation of latitudinal asymmetry in a coupled ocean–atmosphere model. *J. Atmos. Sci.* **53**, 3236–3250 (1996).
11. Nigam, S. & Chao, Y. Evolution dynamics of tropical ocean–atmosphere annual cycle variability. *J. Clim.* **9**, 3187–3205 (1996).
12. Erb, M. P. et al. Response of the equatorial Pacific seasonal cycle to orbital forcing. *J. Clim.* **28**, 9258–9276 (2015).
13. Luan, Y., Braconnot, P., Yu, Y., Zheng, W. & Marti, O. Early and mid-Holocene climate in the tropical Pacific: seasonal cycle and interannual variability induced by insolation changes. *Clim. Past* **8**, 1093–1108 (2012).
14. Karamperidou, C., Di Nezio, P. N., Timmermann, A., Jin, F. F. & Cobb, K. M. The response of ENSO flavors to mid-Holocene climate: implications for proxy interpretation. *Paleoceanography* **30**, 527–547 (2015).
15. Neelin, J. D. et al. ENSO theory. *J. Geophys. Res.* **103**, 14261–14290 (1998).
16. Battisti, D. S. Dynamics and thermodynamics of a warming event in a coupled tropical atmosphere ocean model. *J. Atmos. Sci.* **45**, 2889–2919 (1988).
17. Boos, W. R. & Korty, R. L. Regional energy budget control of the intertropical convergence zone and application to mid-Holocene rainfall. *Nat. Geosci.* **9**, 892–897 (2016).
18. Sobel, A. H., Nilsson, J. & Polvani, L. M. The weak temperature gradient approximation and balanced tropical moisture waves. *J. Atmos. Sci.* **58**, 3650–3665 (2001).
19. Kang, S. M., Held, I. M., Frierson, D. M. W. & Zhao, M. The response of the ITCZ to extratropical thermal forcing: idealized slab-ocean experiments with a GCM. *J. Clim.* **21**, 3521–3532 (2008).
20. Chiang, J. C. H. & Friedman, A. R. Extratropical cooling, interhemispheric thermal gradients, and tropical climate change. *Ann. Rev. Earth Planet. Sci.* **40**, 383–412 (2012).
21. Thomson, D. J. The seasons, global temperature, and precession. *Science* **268**, 59–68 (1995).
22. Koutavas, A., Demenocal, P. B., Olive, G. C. & Lynch-Stieglitz, J. Mid-Holocene El Nino-Southern Oscillation (ENSO) attenuation revealed by individual foraminifera in eastern tropical Pacific sediments. *Geology* **34**, 993–996 (2006).
23. Cobb, K. M. et al. Highly variable El Nino-Southern Oscillation throughout the Holocene. *Science* **339**, 67–70 (2013).
24. Carre, M. et al. Holocene history of ENSO variance and asymmetry in the eastern tropical Pacific. *Science* **345**, 1045–1048 (2014).
25. Emile-Geay, J. et al. Links between tropical Pacific seasonal, interannual and orbital variability during the Holocene. *Nat. Geosci.* **9**, 168–173 (2016).
26. Thompson, D. M. et al. Tropical Pacific climate variability over the last 6000 years as recorded in Bainbridge Crater Lake, Galapagos. *Paleoceanography* **32**, 903–922 (2017).
27. White, S. M., Ravelo, A. C. & Polissar, P. J. Dampened El Nino in the Early and Mid-Holocene due to insolation-forced warming/deepening of the thermocline. *Geophys. Res. Lett.* **45**, 316–326 (2018).
28. Koutavas, A. & Joanides, S. El Nino-Southern Oscillation extrema in the Holocene and Last Glacial Maximum. *Paleoceanography* https://doi.org/10.1029/2012pa002378 (2012).
29. Thirumalai, K., Partin, J. W., Jackson, C. S. & Quinn, T. M. Statistical constraints on El Nino Southern Oscillation reconstructions using individual foraminifera: a sensitivity analysis. *Paleoceanography* **28**, 401–412 (2013).
30. Zhu, J. et al. Reduced ENSO variability at the LGM revealed by an isotope-enabled Earth system model. *Geophys. Res. Lett.* **44**, 6984–6992 (2017).
31. Battisti, D. S. & Hirst, A. C. Interannual variability in a tropical atmosphere ocean model—influence of the basic state, ocean geometry and nonlinearity. *J. Atmos. Sci.* **46**, 1687–1712 (1989).
32. Tziperman, E., Zebiak, S. E. & Cane, M. A. Mechanisms of seasonal–ENSO interaction. *J. Atmos. Sci.* **54**, 61–71 (1997).
33. Cane, M. A. A role for the Tropical Pacific. *Science* **282**, 59–61 (1998).
34. Chiang, J. C. H. The tropics in paleoclimate. *Ann. Rev. Earth Planet. Sci.* **37**, 263–297 (2009).
35. Prell, W. L. & Kutzbach, J. E. Monsoon variability over the past 150,000 years. *J. Geophys. Res.* **92**, 8411–8425 (1987).
36. Wang, Y. J. et al. Millennial- and orbital-scale changes in the East Asian monsoon over the past 224,000 years. *Nature* **451**, 1090–1093 (2008).
37. Hays, J. D., Imbrie, J. & Shackleton, N. J. Variations in Earths orbit—pacemaker of Ice Ages. *Science* **194**, 1121–1132 (1976).
38. Berger, A. Milankovitch theory and climate. *Rev. Geophys.* **26**, 624–657 (1988).
39. Cheng, H. et al. Ice Age terminations. *Science* **326**, 248–252 (2009).
40. Tabor, C. R. et al. Interpreting precession-driven delta O-18 variability in the South Asian monsoon region. *J. Geophys. Res.* **123**, 5927–5946 (2018).
41. Pawlowicz, R. M_Map: A mapping package for MATLAB, version 1.4m (UBC EOAS, 2020); www.eoas.ubc.ca/~rich/map.html
42. Wessel, P. & Smith, W. H. F. A global, self-consistent, hierarchical, high-resolution shoreline database. *J. Geophys. Res.* **101**, 8741–8743 (1996).

Methods

Earth System Model simulations

GFDL CM 2.1. The simulations are as reported in ref. [12]. The GFDL CM 2.1 (ref. [43]) is used at 2° × 2.5° in the atmosphere and 1° × 1° in the ocean but progressively to one-third degree resolution in the meridional direction at the equator. Boundary conditions are set to pre-industrial levels, except for eccentricity which is set to $e = 0.0493$ and LOP to 0°, 90°, 180° and 270°, respectively (labelled AE, WS, VE and SS in ref. [12]). Obliquity is set to 23.439°. A simulation with zero eccentricity is also done. Each simulation is 600 years long and the average of the last 100 years used for the monthly climatology. The calendar was converted to fixed angle from the standard monthly mean output using the method of ref. [44].

iCESM 1.2. The simulations are as reported in ref. [40]. This model uses CESM 1.2 but with the inclusion of a water isotope tracer[45]. The water isotope tracers do not affect the physical climate, so the simulated physical climate is comparable to the CESM 1.2 which has been shown to well-simulate historical and present-day climate[46]. The atmosphere and land are on a 1.9° × 2.5° finite-volume grid and ocean and sea ice on a nominal 1° rotated pole grid (gx1v6). Orbital configurations are as in the AE, WS, VE and SS cases in ref. [12], with eccentricity set to 0.0493 and obliquity to 23.44107°. Other boundary conditions are set to pre-industrial levels. A fifth simulation is performed with eccentricity set to zero. Simulations were run for a total of 1,050 years. The first 500 years were run using CESM 1.2 without water isotope tracers followed by a further 550 years using water isotope tracers. All simulations are near equilibrium with top-of-atmosphere radiation imbalances less than 0.15 W m^{-2}. For this study, all five simulations were extended for 50 years and those data were used to calculate the climatology. The calendar was converted to fixed angle using daily data, following the calendar conversions of ref. [44].

HadCM3. The simulations use the version HadCM3B_M2.1N (ref. [47]). This is a version of the original HadCM3 model[48,49]. The atmospheric component HadAM3B has a Cartesian grid with a horizontal resolution of 96 × 73 grid points (3.75° longitude × 2.5° latitude) and the ocean component has a resolution of 288 × 144 grid points (1.25° longitude × 1.25° latitude). Boundary conditions are set to pre-industrial levels, except for eccentricity which is set to $e = 0.0493$ and the longitude of perihelion set to 0°, 90°, 180° and 270°, respectively. Obliquity is set to pre-industrial level at 23.439°. A simulation with zero eccentricity is also done. Each simulation is 500 years long and the average of the last 100 years is used to form the monthly climatology.

EC Earth. We use the Pmin, Pmax and Tmin simulations of EC Earth as performed in ref. [50]. EC Earth 2.2 is a fully coupled model with an atmospheric horizontal resolution of T159 (roughly 1.125° × 1.125°) and 62 vertical levels and ocean model at 1° resolution and 42 vertical levels. The Pmin simulation sets obliquity at 22.08°, eccentricity at 0.056 and LOP at 264.04°; the Pmax simulation has the same obliquity, eccentricity at 0.058 and LOP at 86.5°. The eccentricity is thus slightly larger than the simulations shown in Fig. 2 and the LOP is not exactly at 270° and 90° but sufficiently close for our purposes for a qualitative comparison. The Tmin simulation is a zero eccentricity simulation with obliquity set to 22.08°, to be compared to the $e = 0$ simulations in Fig. 2. Each simulation is 100 years and the last 50 years is used to form the climatology.

CESM LOP and idealized simulations. Simulations are done with CESM 1.2 (ref. [46]) at 1.9° × 2.5° finite-volume grid and ocean and sea ice on a nominal 1° rotated pole grid (gx1v6). Each simulation is for 25 years and the last 20 years are averaged to form a seasonal climatology. Simulations varying the LOP are done at intervals of 30° from 0° to 330° and for three eccentricities: 0.01, 0.02 and 0.04. Obliquity is set to 23.439°. All other boundary conditions are set to pre-industrial levels. Note that the simulated cold tongue changes here are qualitatively like the longer iCESM 1.2 simulations, despite the short integration time (Extended Data Fig. 9). There are also four idealized simulations: tilt and distance, for which eccentricity is set to 0.05 and obliquity to 23.439° (and LOP = 0°); tilt-only, for which eccentricity is set to zero and obliquity to 23.439°; distance-only, for which obliquity is set to zero and eccentricity to 0.05 (and LOP = 0°); and zero annual forcing for which both obliquity and eccentricity are set to zero. See Extended Data Table 1 for a list of simulations.

Fixed-angle calendar. A calendar adjustment was applied to the CESM LOP and idealized simulations to account for the shift in some dates of equinoxes and solstices when LOP is altered under high eccentricity[51], by assigning each month to 30° of arc in the orbit. The method of ref. [44] was used to alter monthly mean output from the standard calendar to fixed angle, using the vernal equinox as the tie point. The GFDL CM 2.1 and iCESM 1.2 calendars were already converted to fixed angle from their respective original applications[12,40]. The conversion results in a relatively minor modification to the numerical timing of the months; for this reason, the HadCM3 and EC Earth calendars were not converted to fixed angle, noting that those outputs were only used for a qualitative comparison.

Surface fitting

The surface fit of Fig. 3a (and Extended Data Fig. 4a,c) using equation (1) is done in MATLAB R2021a using the function 'fit' and specifying equation (1) as the model using the function 'fittype', setting m and LOP as the independent variables; otherwise, default settings are used. Both functions are found in the curve fitting toolbox[52]. The method uses a nonlinear least squares minimization algorithm (trust-region reflective method) to determine the fit; amplitudes (A_T, A_D and A_S) are allowed to range between 0 and 3 K and phase (p_T, p_D and p_S) between 0 and 12.

Calculation of equatorial thermocline temperature

We first extract the depth of the 20 °C isotherm in the annual mean climatological potential temperature averaged between 6° N and 6° S. There is a depth value for each longitude point across the equatorial Pacific and we use this as the reference thermocline depth. Using monthly climatological potential temperature, we then extract the potential temperature (averaged between 6° S and 6° N) at the reference thermocline depth. For each longitude point, we obtain 12 potential temperature values representing the monthly climatological variation in potential temperature at mean thermocline depth.

Simulations with an ICM of the tropical Pacific

We use an ICM (ref. [16]) of the tropical Pacific coupled ocean–atmosphere system which has been extensively used for ENSO studies. It is an anomaly model and the mean state is prescribed. The atmosphere is a Gill[53] model representing the global tropical atmosphere and with heating parameterized to SST and to convergence feedback. The ocean model is a reduced-gravity 1.5-layer model with an embedded mixed layer and spans only across the tropical Pacific (124° E – 80° W). The atmosphere is coupled to the ocean through wind stress and the reverse through SST. The reader is referred to ref. [16] for details. External wind forcing on the ICM is applied similar to the method used in ref. [54], except that in this case the wind forcing is annually repeating.

We first generate distance effect wind forcing for the ICM by running two CESM 1.2 simulations with $e = 0$ and 0.04 respectively; LOP is set to 0°, obliquity to 23.439° and all other boundary conditions to pre-industrial levels. The CESM 1.2 simulations here use the thermodynamic 'slab' ocean rather than the full dynamical ocean; this allows for the simulation of tropical Pacific climate changes to the orbital forcing in the absence of the ocean–atmosphere dynamics as contained in the ICM. Simulations are 25 years long, with the last 20 used to form the monthly climatology. We extract the distance effect wind forcing from the difference ($e = 0.04$ minus $e = 0$) of the lowest atmospheric level winds from the respective climatologies. The resulting annually repeating wind

forcing is then imposed as an external forcing to the ICM domain. The ICM is run for 100 years and results are averaged over the last 50 years to form the monthly climatological fields shown in Extended Data Fig. 7.

Atmospheric energy flux analysis

The atmospheric energy flux potential analysis[17,55] relates zonal and meridional shifts in tropical rainfall to horizontal atmospheric energy transports, a two-dimensional generalization of the zonal mean energetic approaches[19]. An energy flux potential χ is defined such that its gradient is the divergent component of the horizontal atmospheric energy transport:

$$(\partial_x \chi,\ \partial_y \chi) = (u_h,\ v_h) \tag{2}$$

where x and y are coordinates in the zonal and meridional directions respectively, and u_h and v_h are the zonal and meridional components of the divergent atmospheric energy transport, respectively. The energy flux potential is approximately related to the energy flux into the atmospheric column as (see ref. [17] for a derivation)

$$\nabla^2 \chi \approx E + H + R \tag{3}$$

in which E is the surface latent heat flux, H is the surface sensible heat flux and R is the column radiative heating (the sum of the top of the atmosphere and surface shortwave and longwave energy fluxes) for which the fluxes are defined as positive when directed into the atmosphere. The ascending branches of both meridional and zonal overturning circulations occur along an energy flux equator and EFPM, respectively. An energy flux equator is a latitude for which $v_h = 0$ and $\partial_y v_h > 0$ and an EFPM is a longitude for which $u_h = 0$ and $\partial_x u_h > 0$.

To calculate the energy flux potential, we first calculated the monthly mean net energy input into the atmospheric column using the sum of surface latent heat flux, surface sensible heat flux and surface and top-of-atmosphere longwave and shortwave radiation fluxes. The Laplacian solver from the windspharm Python package[56] is then used to solve the Laplace equation (3) on a spherical surface. We then used the package's gradient function to calculate u_h and v_h for each month from the corresponding energy flux potential. To calculate the EFPM shown in Fig. 4a, u_h is averaged between 10° S and 10° N, and a five-point smoothing is applied twice longitudinally to the resulting field. The EPFM is then identified, for each month, at the longitude for which $u_h = 0$.

Data availability

The iCESM 1.2, HadCM3, CESM 1.2 and ICM output variables used in this study are available at ref. [57] (https://doi.org/10.6078/D1VB0G). GFDL CM 2.1 model output is available at ref. [58] and EC Earth output at ref. [59].

Code availability

The CESM 1.2 code is publicly available at https://www.cesm.ucar.edu/models/cesm1.2/. Analytical codes used in this paper are available in ref. [57] (https://doi.org/10.6078/D1VB0G).

43. Delworth, T. L. et al. GFDL's CM2 global coupled climate models. Part I: Formulation and simulation characteristics. *J. Clim.* **19**, 643–674 (2006).
44. Pollard, D. & Reusch, D. B. A calendar conversion method for monthly mean paleoclimate model output with orbital forcing. *J. Geophys. Res.* https://doi.org/10.1029/2002jd002126 (2002).
45. Brady, E. et al. The connected isotopic water cycle in the Community Earth System Model Version 1. *J. Adv. Model. Earth Syst.* **11**, 2547–2566 (2019).
46. Hurrell, J. W. et al. The Community Earth System Model: a framework for collaborative research. *Bull. Am. Meteorol. Soc.* **94**, 1339–1360 (2013).
47. Valdes, P. J. et al. The BRIDGE HadCM3 family of climate models: HadCM3@Bristol v1.0. *Geosci. Model Dev.* **10**, 3715–3743 (2017).
48. Pope, V. D., Gallani, M. L., Rowntree, P. R. & Stratton, R. A. The impact of new physical parametrizations in the Hadley Centre climate model: HadAM3. *Clim. Dynam.* **16**, 123–146 (2000).
49. Gordon, C. et al. The simulation of SST, sea ice extents and ocean heat transports in a version of the Hadley Centre coupled model without flux adjustments. *Clim. Dynam.* **16**, 147–168 (2000).
50. Bosmans, J. H. C., Drijfhout, S. S., Tuenter, E., Hilgen, F. J. & Lourens, L. J. Response of the North African summer monsoon to precession and obliquity forcings in the EC-Earth GCM. *Clim. Dynam.* **44**, 279–297 (2015).
51. Joussaume, S. & Braconnot, P. Sensitivity of paleoclimate simulation results to season definitions. *J. Geophys. Res.* **102**, 1943–1956 (1997).
52. Curve Fitting Toolbox v.3.6 (Natick, 2020).
53. Gill, A. E. Some simple solutions for heat-induced tropical circulation. *Q. J. R. Meteorol. Soc.* **106**, 447–462 (1980).
54. Thomas, E. E. & Vimont, D. J. Modeling the mechanisms of linear and nonlinear ENSO responses to the Pacific meridional mode. *J. Clim.* **29**, 8745–8761 (2016).
55. Lintner, B. R. & Boos, W. R. Using atmospheric energy transport to quantitatively constrain South Pacific convergence zone shifts during ENSO. *J. Clim.* **32**, 1839–1855 (2019).
56. Dawson, A. Windspharm: a high-level library for global wind field computations using spherical harmonics. *J. Open Res. Softw.* **4**, e31 (2016).
57. Chiang, J. C. H., Vimont, D. J., Nicknish, P. A., Roberts, W. H. G. & Tabor, C. R. Data and Code associated with: two annual cycles of the Pacific cold tongue under orbital precession. *Dryad* https://doi.org/10.6078/D1VB0G (2022).
58. Erb, M., Broccoli, A. & Raney, B. Idealized single-forcing GCM simulations with GFDL CM2.1. *Zenodo* https://doi.org/10.5281/zenodo.1194480 (2018).
59. Bosmans, J. Idealized orbital extreme GCM simulations with EC-Earth-2-2. *Zenodo* https://doi.org/10.5281/zenodo.3268528 (2019).
60. Dee, D. P. et al. The ERA-Interim reanalysis: configuration and performance of the data assimilation system. *Q. J. R. Meteorol. Soc.* **137**, 553–597 (2011).

Acknowledgements We thank D. Battisti for providing the ICM code, W. Boos for providing code for the energy flux diagnostic, D. Pollard and M. Erb for providing code for the fixed-angle calendar conversion, S. White and R. Shen for advice on palaeoproxy records, and B. Raney and J. Bosmans for providing the GFDL and EC Earth model output, respectively. J.C.H.C. acknowledges support from a Visiting Professorship at Academia Sinica, funded by the Ministry of Science and Technology, Taiwan, under grant no. 110-2811-M-001-554. A.R.A. acknowledges support from National Science Foundation award 1903640. C.R.T. acknowledges funding from the National Center for Atmosphere Research Advanced Study Program postdoctoral fellowship. This research used the Savio computational cluster resource provided by the Berkeley Research Computing program at the University of California, Berkeley (supported by the UC Berkeley Chancellor, Vice Chancellor for Research and Chief Information Officer). High-performance computing support on Cheyenne (https://doi.org/10.5065/D6RX99HX) was provided by NCAR's Computational and Information Systems Laboratory, sponsored by the National Science Foundation.

Author contributions J.C.H.C., A.R.A. and A.J.B. conceived the study. J.C.H.C. conducted the CESM simulations and led the data analysis, writing of the manuscript and design of figures. D.J.V. and A.R.A. undertook the ICM simulations and analysis. P.A.N. provided the energy flux analysis. W.H.G.R. and C.R.T. conducted the HadCM3 and iCESM1.2 model simulations, respectively. All authors contributed to the writing of this manuscript.

Competing interests The authors declare no competing interests.

Additional information

Correspondence and requests for materials should be addressed to John C. H. Chiang.

Peer review information *Nature* thanks Shang-Ping Xie and the other, anonymous, reviewer(s) for their contribution to the peer review of this work.

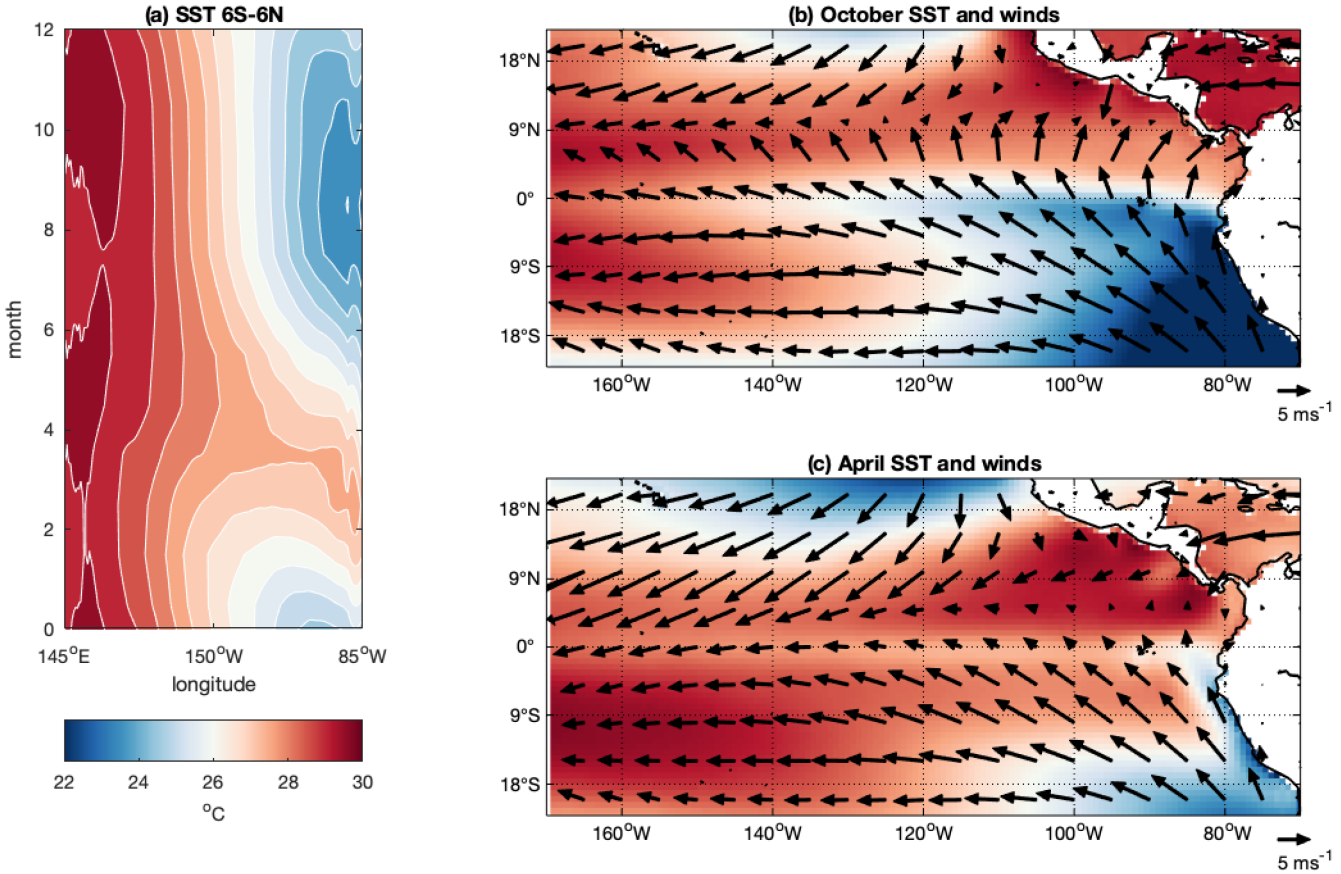

Extended Data Fig. 1 | Modern-day observed Pacific cold tongue annual cycle. (**a**) SST averaged over 6°S–6°N, showing the cold tongue annual cycle with the cold peak in boreal fall and warm peak in boreal spring. Note that the time axis is such that 0 is the start of the year and 12 is the end; mid-January is thus 0.5. (**b**-**c**) SST and 10m winds for (**b**) October (cold peak), and (**c**) April (warm peak). Data is from ERA-Interim[60], averaged over 1979–2018. The M_Map package[41] is used to generate the maps for (b) and (c), using coastline data from the Global Self-consistent, Hierarchical, High-resolution Geography Database[42].

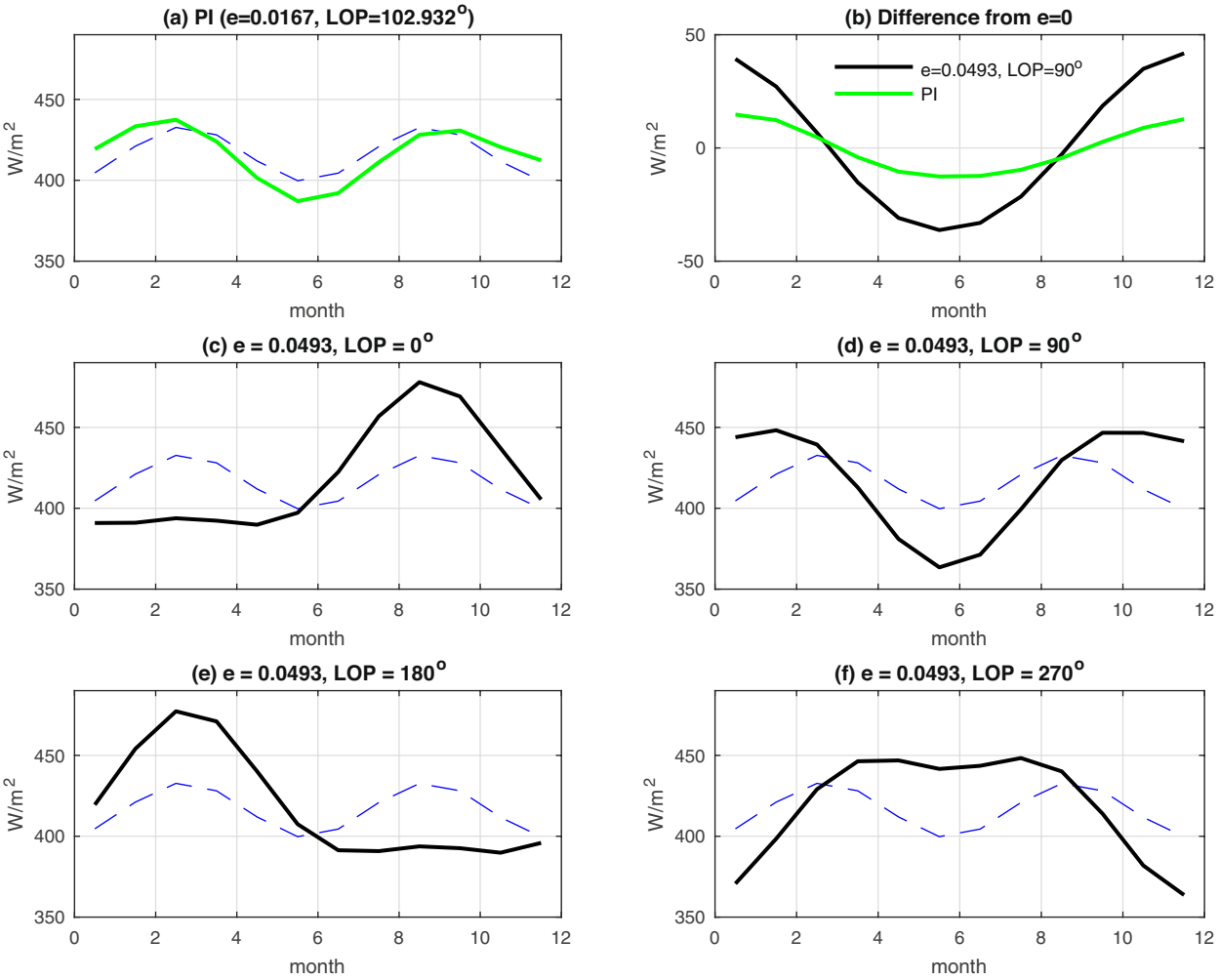

Extended Data Fig. 2 | The seasonal cycle of insolation at the equator for different orbital configurations, including those used in Fig. 2. In all cases, downward solar radiation at top-of-atmosphere is averaged over 6°S–6°N, and the blue dashed line is for the tilt-only (e = 0) case. (**a**) Pre-industrial case. (**b**) difference from the tilt-only case for LOP = 90°, e = 0.0493 (black line), and pre-industrial (green line). (**c**) LOP = 0°, e = 0.0493. (**d**) LOP = 90°, e = 0.0493. (**e**) LOP = 180°, e = 0.0493. (**f**) LOP = 270°, e = 0.0493. Insolation data is from the GFDL CM 2.1 simulations of Erb et al. (2015)[12]. Panel (b) shows the contrast in the amplitude of insolation changes between the e = 0.0493 case (~ 42W/m^2) and the pre-industrial case (~15W/m^2) where the eccentricity is ~1/3 as large.

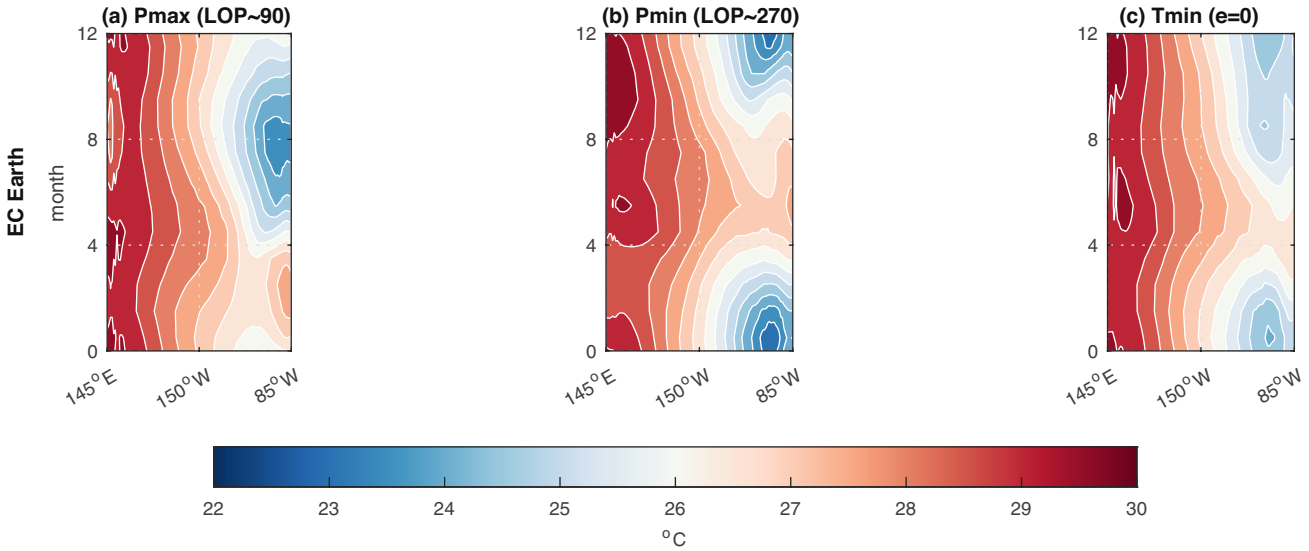

Extended Data Fig. 3 | Cold tongue annual cycle in EC Earth also shows consistent variation with changing LOP. Plotted is the climatological monthly mean SST averaged over 6°S–6°N (same as Fig. 2) for the (**a**) Precession maximum, minimum obliquity (Pmax), (**b**) Precession minimum, minimum obliquity (Pmin), and (**c**) Minimum obliquity with circular orbit (Tmin) runs in Bosmans et al. (2015)[50]. To facilitate comparison, an offset is added to each panel so that the annual mean SST averaged over 145–275°E is the same as for the observational data as shown in Extended Data Fig. 1a, 27.44 °C. The orbital parameters are slightly different, but Pmax corresponds approximately to the LOP = 90° simulation, Pmin to LOP = 270° simulation, and Tmin to the e = 0 simulation. The column positioning of the panels corresponds to the equivalent LOP or e = 0 case in Fig. 2. See Methods section on 'Earth System Model simulations' for the orbital parameters and details of the simulations.

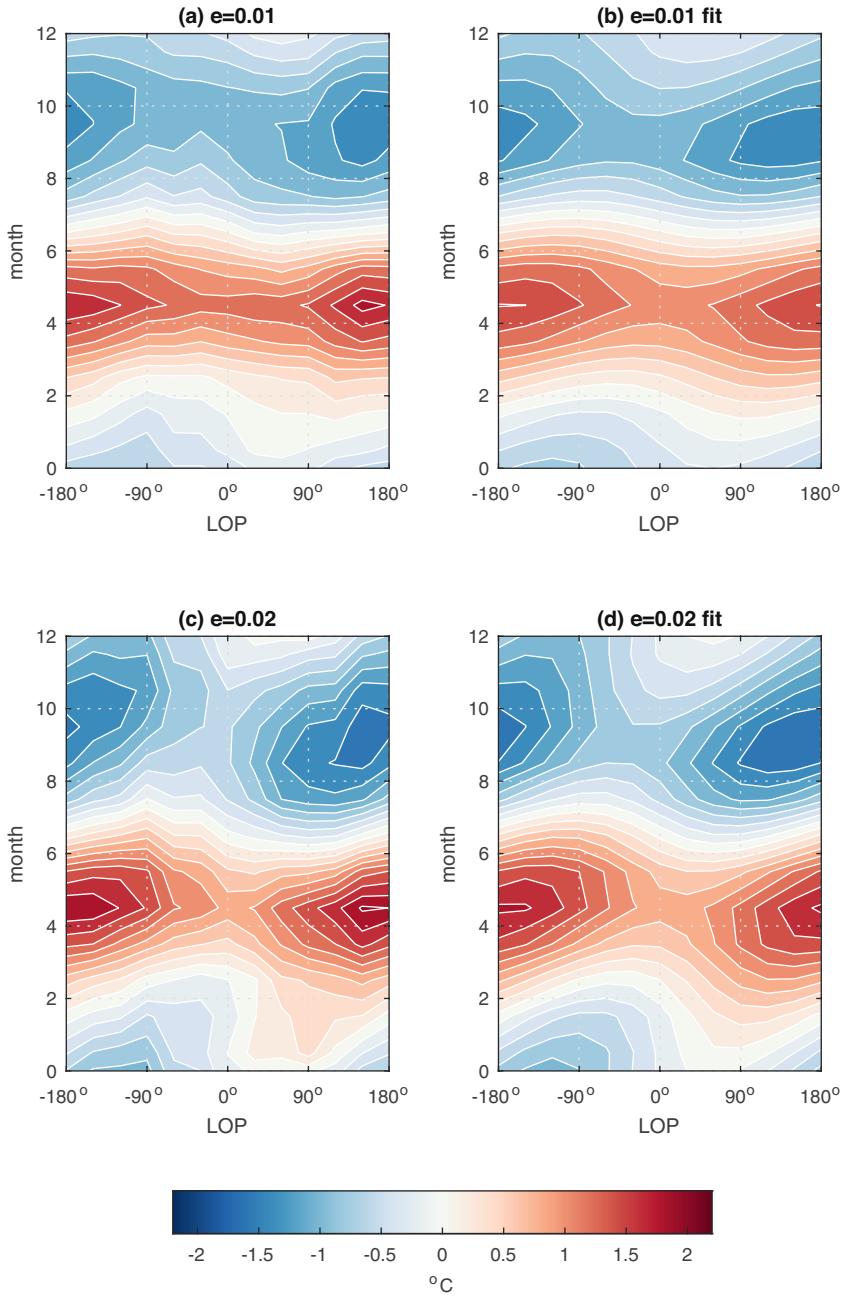

Extended Data Fig. 4 | Variation of the cold tongue SST annual cycle to LOP in CESM LOP for e = 0.01 and e = 0.02, and their fits to equation 1. (**a**) Cold tongue SST (averaged over 6°S–6°N, 140–90°W) for e = 0.01 and varying longitude of perihelion. The annual mean is removed before plotting. (**b**) Least-square surface fit of the data in (a), using equation 1. (**c**) and (**d**): same as (a) and (b) respectively, except for e = 0.02. See Table 1 for the fitted coefficients.

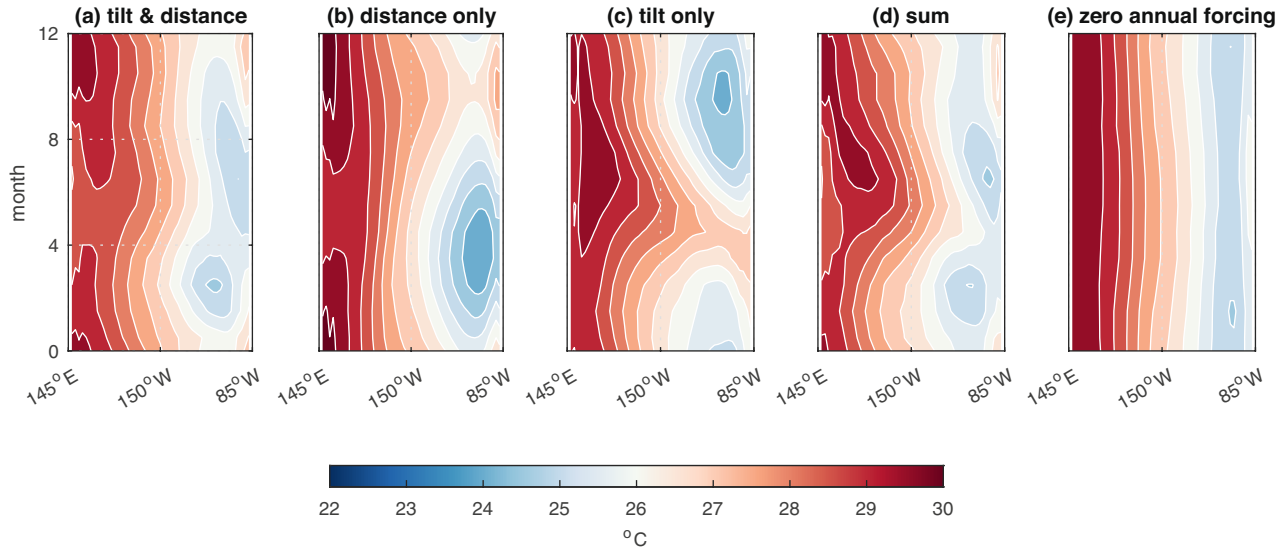

Extended Data Fig. 5 | CESM 1.2 annual cycle of equatorial Pacific SST under different combinations of tilt and distance effects. Plotted is climatological monthly mean SST averaged over 6°S–6°N across the Pacific. In all cases, LOP = 0°. To facilitate comparison, an offset is added to each panel so that the annual mean SST averaged over 145°E–85°W is the same as for the observational data as shown in Extended Data Fig. 1a, 27.44 °C. (**a**) e = 0.05, obliquity = 23.439° (tilt and distance run); (**b**) e = 0.05, obliquity = 0° (distance-only run); (**c**) e = 0.00, obliquity = 23.439° (tilt-only run); (**d**) sum of the annual cycles of (b) and (c), added to the annual mean of (a); and (**e**) e = 0, obliquity = 0° (zero annual forcing run).

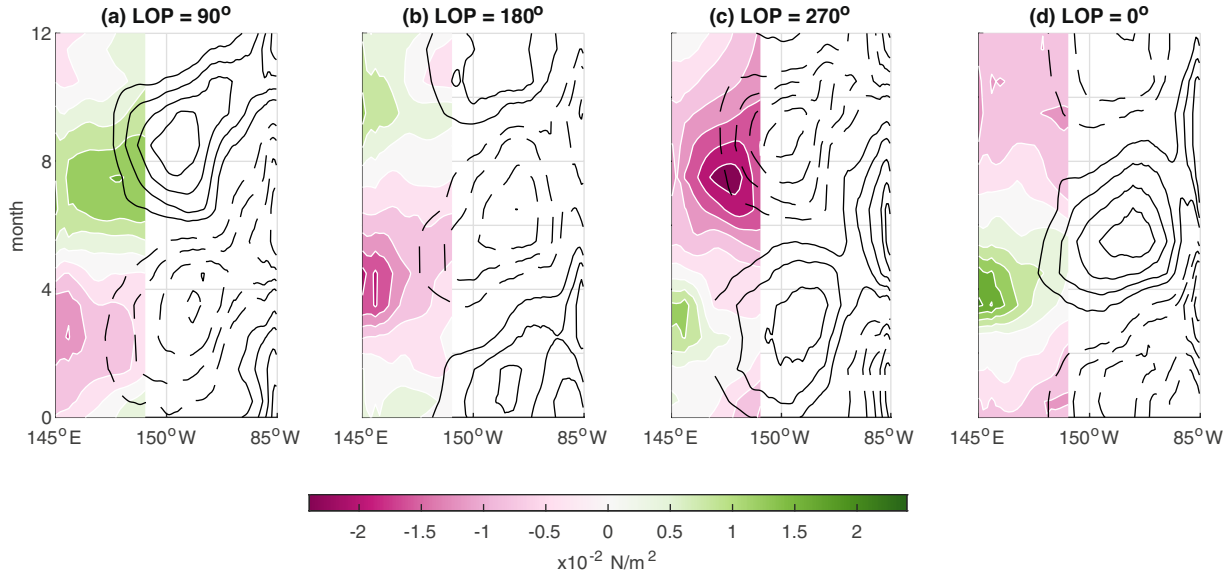

Extended Data Fig. 6 | Equatorial thermocline response in the CESM LOP simulations connects the western equatorial Pacific zonal wind stress change to cold tongue changes. LOP cases (**a**) 90°, (**b**) 180°, (**c**) 270°, and (**d**) 0° are shown. **Contours** show the 6°S–6°N averaged temperature anomaly at mean thermocline depth for e = 0.04, for the stated LOP. The temperature averaged across all LOP cases is first subtracted out, to remove the influence of the tilt effect from the thermocline. The contour interval is 0.5K, and dashed values are negative; the zero contour is not shown. For clarity, only values east of 170°E are plotted. The eastward propagation of thermocline anomalies is visually apparent. Shading represents the corresponding zonal wind stress anomaly averaged over 6°S–6°N; the average across all LOP cases is first subtracted out, to remove the influence of the tilt effect. Only values in the western Pacific (west of 160°W) are plotted. Positive values indicate westerlies. Although only four LOP cases are shown here, a deeper thermocline (as indicated by warmer temperature) in the western Pacific is accompanied by a westerly wind stress anomaly (and vice versa) for all LOP cases.

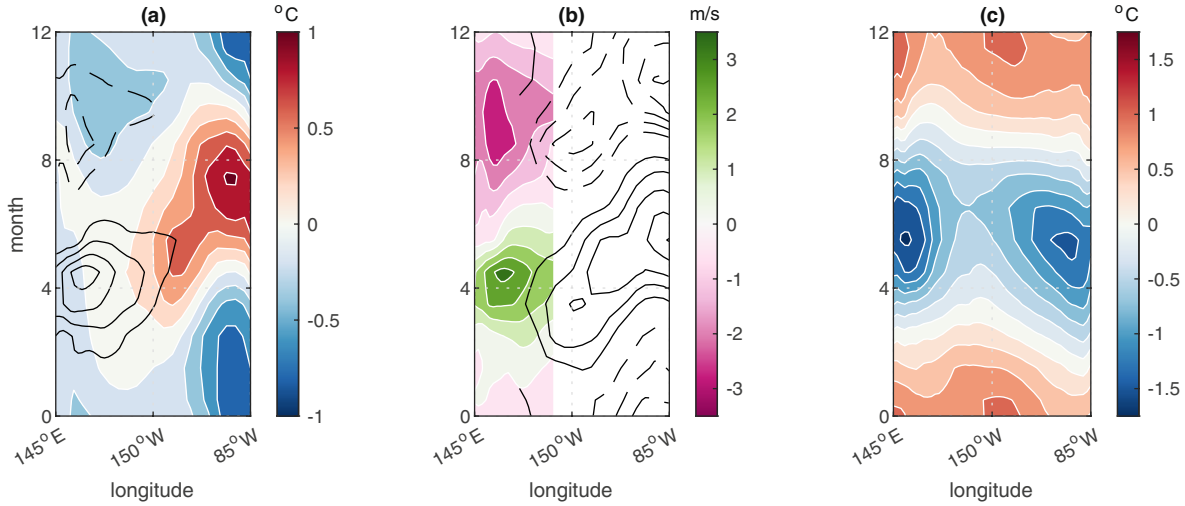

Extended Data Fig. 7 | An intermediate coupled model (ICM) with imposed distance effect annually-varying wind forcing generates a cold tongue annual cycle. All fields as shown are averaged over 6°S–6°N. (**a**) Distance effect zonal wind anomalies from the lowest model level of the CESM 1.2 coupled to a slab ocean (contour interval 0.75m/s, dashed contours are negative, zero contour omitted) and the SST response of the ICM to the applied wind forcing (shaded). This shows the cold tongue annual cycle in SST generated by the winds. (**b**) Full zonal wind (CESM 1.2 slab ocean + ICM) anomalies up to 160°W (shaded) and ICM thermocline depth anomalies east of 170°E (contour interval 2m, dashed contours are negative, zero contour omitted). This shows the connection between the winds and the cold tongue through thermocline changes. (**c**) SST anomalies due to the distance effect orbital forcing in the CESM 1.2 coupled to a slab ocean, showing the peak warming around December from the thermodynamic response to the distance effect insolation. The magnitude of the SST change here is not directly comparable with that of the ICM in panel (a), because of the lack of ocean dynamical feedback in the slab ocean that would alter the thermodynamic SST response. See Methods section on 'Simulations with an ICM of the tropical Pacific' for details.

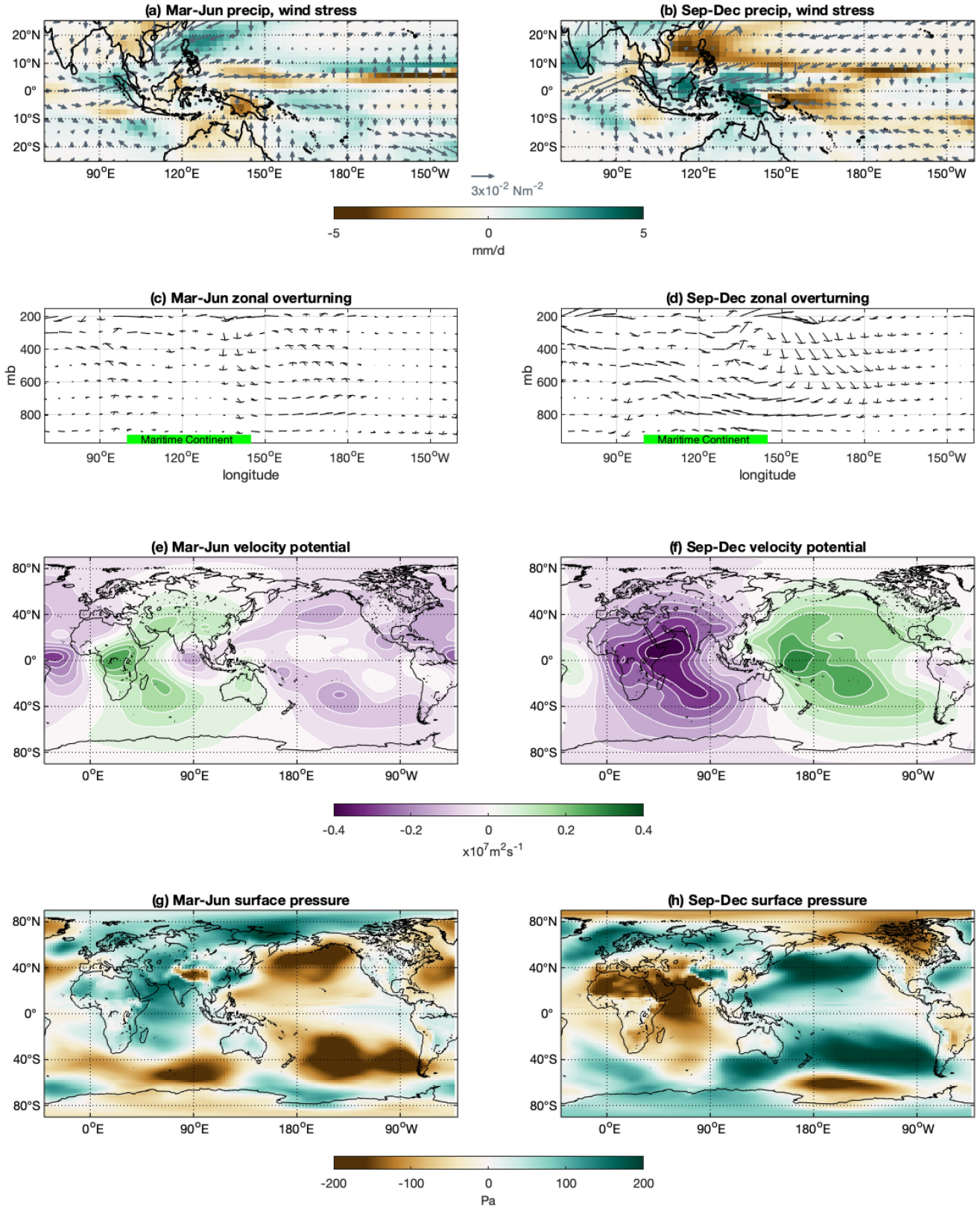

Extended Data Fig. 8 | See next page for caption.

Extended Data Fig. 8 | Seasonal longitudinal shift in the Walker circulation due to the distance effect. The difference between the distance-only run and zero annual forcing run (former minus latter) for various climate fields averaged over March–June (following aphelion) in the left column, and September–December (following perihelion) in the right column. (**a**-**b**) Precipitation (shaded) and wind stress (vectors). (**c**-**d**) Zonal overturning circulation at the equator displayed as vectors, with the x-component being the divergent component of the zonal wind (in m/s) averaged 10°S-10°N and y-component being the pressure vertical velocity (in Pa/s) multiplied by 250, also averaged 10°S-10°N. The green bar in (c-d) indicates the approximate longitudes of the Maritime Continent. (**e**-**f**) 200mb velocity potential. (**g**-**h**) Surface pressure. The precipitation in panels (a-b) show a shift in the location of equatorial rainfall between the Maritime Continent and western equatorial Pacific between March–June and September–December, associated with changing equatorial trades over the western equatorial Pacific. The zonal overturning circulation in panels (c-d) show anomalous subsidence over the Maritime continent and anomalous uplift over the western equatorial Pacific in March–June, indicating an eastward shift in the main uplift region of the Walker circulation; the opposite occurs for September–December. The velocity potential change in panels (e-f) shows a predominantly zonal wavenumber 1 pattern with the nodal point over the Maritime continent, reversing in sign between March–June and September–December. The surface pressure change in panels (g-h) show a see-saw in atmospheric mass between Africa/Indian ocean and the Pacific, again with the nodal point at the Maritime continent. Thus, all fields shown are consistent with a seasonal longitudinal shift of the Walker circulation towards the east in March–June and towards the west in September–December. The M_Map package[41] is used to generate the maps, using coastline data from the Global Self-consistent, Hierarchical, High-resolution Geography Database[42].

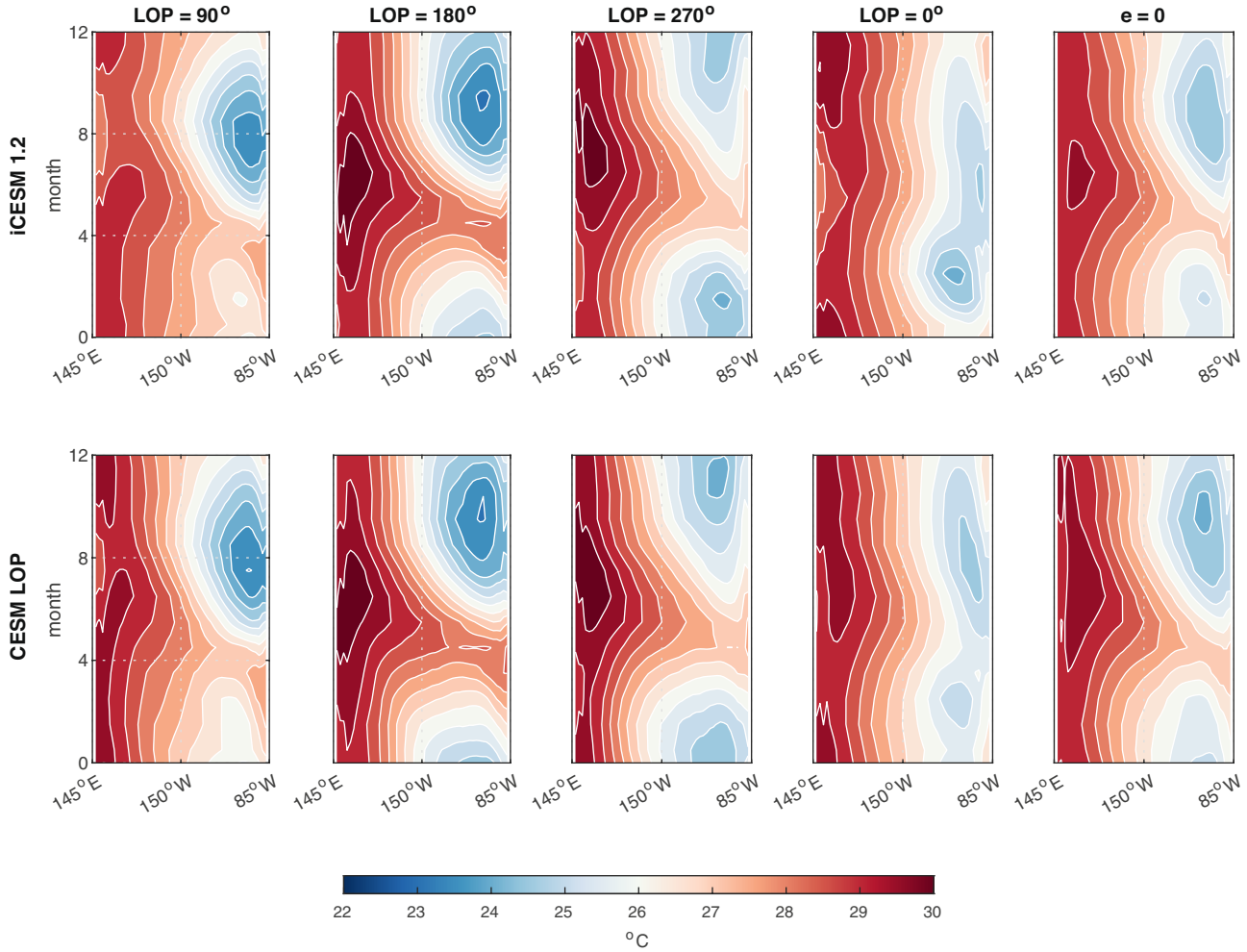

Extended Data Fig. 9 | Consistent cold tongue annual cycle changes between the iCESM 1.2 and CESM LOP simulations. Plotted is the climatological monthly mean SST averaged over 6°S–6°N, for (top row) iCESM 1.2[40], and (2rd row) CESM LOP. The numbers on the top row denote the longitude of perihelion (where 90° = perihelion at winter solstice, 180° = at vernal equinox, 270° = at summer solstice, and 0° = at autumn equinox), and the last column from simulations setting eccentricity to zero. To facilitate comparison, an offset is added to each panel so that the annual mean SST averaged over 145°E–85°W is the same as for the observational data as shown in Extended Data Fig. 1a, 27.44 °C. Despite the short integration time for the CESM LOP, the cold tongue seasonal cycle changes are qualitatively similar with the longer iCESM 1.2 simulations.

Extended Data Table 1 | Summary table of CESM 1.2 simulations used in this study and their orbital configurations

Name of simulation	Eccentricity	Longitude of Perihelion (LOP)	Obliquity
CESM LOP	0.01, 0.02, and 0.04	0° to 330° in steps of 30°	23.439°
Tilt and Distance	0.05	0°	23.439°
Distance-only	0.05	0°	0°
Tilt-only	0.00	0°	23.439°
Zero annual forcing	0.00	0°	0°

All other boundary conditions are set to pre-industrial (1850 AD). All simulations are 25 years long, and the last 20 are used to calculate the climatology. Note that the simulations used for Fig. 2 are not listed here; details of those simulations are in the Methods section on 'CESM LOP and idealized simulations'.